Nodal precession of WASP-33b for 11 yr by Doppler tomographic and transit photometric observations

Watanabe, N.; Narita, N.; Palle, E.; Fukui, A.; Kusakabe, N.; Parviainen, H.; ... ; Kawauchi, K.

Nodal Precession of WASP-33b for Eleven Years by Doppler Tomographic and Transit Photometric Observations

Noriharu Watanabe (iD),[1]* Norio Narita (iD),[2,3,4] Enric Palle (iD),[4,5] Akihiko Fukui (iD),[2,4] Nobuhiko Kusakabe (iD),[3,6] Hannu Parviainen (iD),[4,5] Felipe Murgas (iD),[4,5] Núria Casasayas-Barris (iD),[7] Marshall C. Johnson (iD),[8] Bun'ei Sato (iD),[9] John H. Livingston (iD),[10] Jerome P. de Leon (iD),[10] Mayuko Mori (iD),[10] Taku Nishiumi (iD),[6,11] Yuka Terada (iD),[12,13] Emma Esparza-Borges (iD),[4,5] and Kiyoe Kawauchi (iD)[4]

[1]*Department of Multi-Disciplinary Sciences, Graduate School of Arts and Sciences, The University of Tokyo, 3-8-1 Komaba, Meguro, Tokyo 153-8902, Japan*
[2]*Komaba Institute for Science, The University of Tokyo, 3-8-1 Komaba, Meguro, Tokyo 153-8902, Japan*
[3]*Astrobiology Center, 2-21-1 Osawa, Mitaka, Tokyo 181-8588, Japan*
[4]*Instituto de Astrofísica de Canarias (IAC), E-38200 La Laguna, Tenerife, Spain*
[5]*Dept. Astrofísica, Universidad de La Laguna (ULL), E-38206 La Laguna, Tenerife, Spain*
[6]*National Astronomical Observatory of Japan, 2-21-1 Osawa, Mitaka, Tokyo 181-8588, Japan*
[7]*Leiden Observatory, Leiden University, Postbus 9513, 2300RA Leiden, The Netherlands*
[8]*Department of Astronomy, The Ohio State University, 4055 McPherson Laboratory, 140 West 18th Ave., Columbus, OH 43210 USA*
[9]*Department of Earth and Planetary Sciences, Tokyo Institute of Technology, Meguro-ku, Tokyo, 152-8551, Japan*
[10]*Department of Astronomy, Graduate School of Science, The University of Tokyo, 7-3-1 Hongo, Bunkyo-ku, Tokyo 113-0033, Japan*
[11]*Department of Astronomical Science, The Graduated University for Advanced Studies, SOKENDAI, 2-21-1, Osawa, Mitaka, Tokyo, 181-8588, Japan*
[12]*Institute of Astronomy and Astrophysics, Academia Sinica, P.O. Box 23-141, Taipei 10617, Taiwan, R.O.C.*
[13]*Department of Astrophysics, National Taiwan University, Taipei 10617, Taiwan, R.O.C.*

ABSTRACT

WASP-33b, a hot Jupiter around a hot star, is a rare system in which nodal precession has been discovered. We updated the model for the nodal precession of WASP-33b by adding new observational points. Consequently, we found a motion of the nodal precession spanning 11 years. We present homogenous Doppler tomographic analyses of eight datasets, including two new datasets from TS23 and HIDES, obtained between 2008 and 2019, to illustrate the variations in the projected spin-orbit obliquity of WASP-33b and its impact parameter. We also present its impact parameters based on photometric transit observations captured by MuSCAT in 2017 and MuSCAT2 in 2018. We derived its real spin-orbit obliquity ψ, stellar spin inclination i_s, and stellar gravitational quadrupole moment J_2 from the time variation models of the two orbital parameters. We obtained $\psi = 108.19^{+0.95}_{-0.97}$ deg, $i_s = 58.3^{+4.6}_{-4.2}$ deg, and $J_2 = (1.36^{+0.15}_{-0.12}) \times 10^{-4}$. Our J_2 value was slightly smaller than the theoretically predicted value, which may indicate that its actual stellar internal structure is different from the theoretical one. We derived the nodal precession speed $\dot{\theta} = 0.507^{+0.025}_{-0.022}$ deg year^{-1}, and its period $P_{\text{pre}} = 709^{+33}_{-34}$ years, and found that WASP-33b transits in front of WASP-33 for only ~ 20 % of the entire nodal precession period.

Key words: planet–star interactions — planetary systems — planets and satellites: individual (WASP-33b) — techniques: spectroscopic

1 INTRODUCTION

To date, WASP (Wide Angle Search for Planets; Collier Cameron et al. 2007), KELT (Kilodegree Extremely Little Telescope; Pepper et al. 2007) and TESS (Ricker et al. 2015) surveys have confirmed that there are 17 hot Jupiters around hot stars (> 7000 K). Despite their small number, their orbital obliquities tend to have a wide range. This tendency indicates that they did not experience realignment by the tidal torque (Albrecht et al. 2012). Generally, hot host stars rotate rapidly, yielding oblateness larger than those of slowly rotating stars.

A misaligned orbit and a fast-rotating star force faster precession.At present, there are only two planets whose nodal precessions have been detected: Kepler-13Ab (Szabó et al. 2012) and WASP-33b (Johnson et al. 2015). These planets are hot Jupiters, revolving in misaligned orbits around rapidly rotating hot stars.

WASP-33b, a hot Jupiter ($R_p = 1.5R_J$) around an A-type ($T_{\text{eff}} = 7430 \pm 100$K) and rapidly rotating ($V \sin i_s = 85.6$ km s^{-1}) star, is the only planet whose precession has been detected by Doppler tomography based on transit spectral data. This planet was discovered by Collier Cameron et al. (2010); its nodal precession has been detected by more than one Doppler tomographic measurement (Johnson et al. 2015; Iorio 2016; Watanabe et al. 2020; Borsa et al. 2021). The

* E-mail: n-watanabe@g.ecc.u-tokyo.ac.jp

latest study on this topic (Borsa et al. 2021) derived the angle between the stellar spin axis and line of sight $i_s = 90.11 \pm 0.12$ deg as well as the stellar gravitational quadrupole moment $J_2 = (6.73 \pm 0.22) \times 10^{-5}$ from the measurements; however, the value of i_s does not match that of Iorio (2016) within 3 σ, whereas the value of J_2 is also not consistent with that of Watanabe et al. (2020) within 3 σ. Moreover, (Borsa et al. 2021) revealed that the change in the transit chord of WASP-33b is slightly overly complicated for hereafter estimating the position of the transit chord. Thus, we performed more additional observations and datasets to obtain more accurate values of i_s and J_2, as well as a clearer forecasting of the transit chord.

In this paper, we report the nodal precession of WASP-33b for a longer period of 11 years by considering additional Doppler tomographic measurements obtained through spectral transit and transit photometric observations. Transit photometry is an important method for measuring the impact parameter b and its change, as demonstrated by Szabó et al. (2012), who applied this to detect the nodal precession of Kepler-13Ab using Kepler's photometric datasets. In Section 2, we present our spectral datasets for Doppler tomography and the steps for measuring the orbital parameters, i.e., b and the projected spin-orbit obliquity λ, the angle between the stellar spin axis and the planetary orbital axis. We explain how to handle our transit photometric datasets for determining b in Section 3. Moreover, we fit the values of these two parameters from the spectral and photometric measurements with the nodal precession model, which is described in Section 4. We display the behaviour of WASP-33b's nodal precession and the derived parameters of WASP-33b and its host star in Section 5. In Section 6, we discuss the nodal precession results. Finally, we present our conclusions in Section 7.

2 DOPPLER TOMOGRAPHIC MEASUREMENT

We can simultaneously measure λ and b from the transit spectral data via Doppler tomography. When a planet passes in front of the stellar disk, a bump, referred to as a planetary shadow, appears in the stellar line profile. The orbital configuration of the planet can be derived from this shadow motion.

2.1 Observation Datasets

We used eight spectroscopic datasets for WASP-33 around planetary transits.

One of them was obtained with the High Dispersion Spectrograph (HDS; Noguchi et al. 2002) at the 8.2 m Subaru telescope on 19 October, 2011 UT. The other two datasets were obtained by the Harlan J. Smith Telescope (HJST) with the Robert G. Tull Coudé Spectrograph (TS23; Tull et al. 1995) at McDonald Observatory on 12 November 2008 UT and 4 October 2014 UT. These datasets were also used in our previous study Watanabe et al. (2020). To extract each line profile from each spectrum, we adopted least-squares deconvolution (LSD; Donati et al. 1997); the observed spectrum was regarded as a convolution of a line profile and a series of delta functions. Under this method, we obtained a list of the absorption lines from the Vienna Atomic Line Database (VALD; Kupka et al. 2000) to create a series of delta functions. We then derived each line profile and the error bars with the matrix calculations in Kochukhov et al. (2010).

We then have analysed three spectroscopic datasets obtained on 28 September 2016 UT, 12 January 2018 UT, and 2 January 2019 UT from the high-resolution HARPS-N spectrograph (Cosentino et al. 2012), which is mounted at the Telescopio Nazionale Galileo (TNG).

These three datasets have been extracted and published in Borsa et al. (2021), which were used in the extracted line profile series in this study.

We also We then included two aditional spectral datasets. One was an extracted dataset taken by HJST/TS23 on 11 December 2016 UT. Data from 2016 also included 10 in-transit spectra. The other dataset was obtained from the 188 cm telescope with HIgh Dispersion Echelle Spectrograph (HIDES; Izumiura 1999) at Okayama Astro-Complex (OAC) in Japan on 27 December, 2019 UT. We utilized a wavelength range from 4980Å to 6220Å except for the Na D lines and wavelength regions around bad pixels. We reduced these spectral data by the subtracting bias and dark features, flat dividing, and performing one-dimensional spectrum and wavelength calibration. We then utilized their continua, as well as the HDS process. We selected alp Leo, a rapidly-rotating star ($V \sin i_s \sim 300$ km s^{-1}; Abt et al. 2002), to erase the Earth's atmospheric absorption lines. We then shifted the spectra to the barycentric frame using PyRAF (Science Software Branch at STScI 2012). Finally, we extracted each line profile of each exposure using the LSD.

2.2 Extracting planetary shadow

We derived a median line profile from all exposure data including in-transit for each epoch. We applied a median line profile, not a mean profile, because it avoided the effects of outliers. We subtracted the median line profile from each exposure line profile to calculate the time-series of the line profile residuals. Both the planetary shadow due to the transit of WASP-33b and a striped pattern due to the non-radial pulsations on the surface of WASP-33 (Collier Cameron et al. 2010) were present in the line profile residuals. Herrero et al. (2011) showed that the pulsation period was approximately 68 min based on photometric observations. However, determining the period from the Doppler tomographic results was difficult owing to the irregular patterns.

To extract only the planetary shadow, we applied a Fourier filtering technique (Johnson et al. 2015) because the planet is retrograde, while the pulsations are prograde. First, we performed a two-dimensional Fourier transform. There were components derived from the pulsations in the Fourier space in the first and third quadrants, and the planetary shadow's components in the second and fourth quadrants. Second, we created a filter in which we set unity in the two diagonal quadrants, including power from the planetary shadow, and zero in the other quadrants, including power from the pulsation with a Hann function between these quadrants. Finally, we multiplied the Fourier space by the filter and performed an inverse Fourier transform on the filtered Fourier space to extract the planetary shadow. Figure 1 illustrates these procedures.

2.3 Deriving parameters

To obtain the best-fit values and uncertainties of the transit parameters, we adopted the Markov chain Monte Carlo (MCMC) method using the code EMCEE (Foreman-Mackey et al. 2013).

We modelled a planetary shadow via a convolution between a rotational broadening profile and a Gaussian line profile owing to intrinsic broadening, thermal broadening, and micro-turbulence. The detailed equations to derive the model of the planetary shadow are described in the appendix of Watanabe et al. (2020). We then applied the same filter to the model of the planetary shadow following the procedures described in Section 2.2.

We fitted the observed residuals of the five datasets to the models
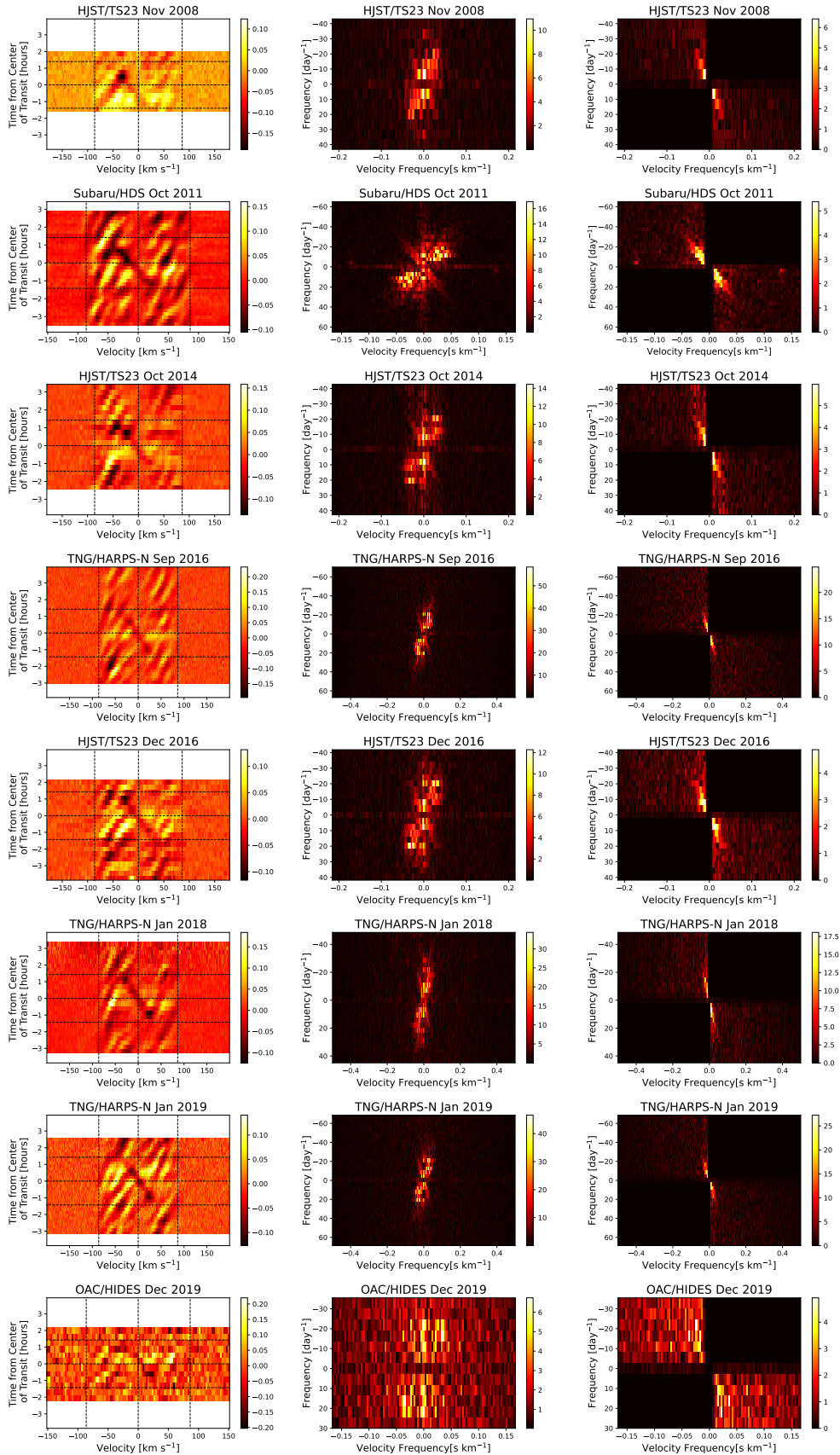
Figure 1. Doppler tomographic datasets and Fourier filters. Left column: observed residuals for the line profile series. The vertical dotted lines show $v = 0$ and $\pm v \sin i_s$. The bottom, middle, and upper horizontal dotted lines show the beginning, middle, and end of the WASP-33b's transit, respectively. Middle column: Fourier spaces after Fourier transform of the residuals for the line profile series. These colour scales are shown as square roots. The faint narrow structure from the bottom right to the upper left is a component of WASP-33b's planetary transit. In contrast, the bright-wide structure from the bottom left to the upper right is a pulsation component. Right column: filtered Fourier space such that only the transit component remains.

Table 1. Details on the spectral datasets

Date (UT)	Instrument	Number of spectra	Exposure time (s)	Resolution	SNR at 5500Å	Reference
12 Nov 2008	HJST/TS23	13	900	60,000	140[†]	Collier Cameron et al. (2010)
19 Oct 2011	Subaru/HDS	35	600 (33 spectra), 480 (2 spectra)	110,000	160[†]	Watanabe et al. (2020)
4 Oct 2014	HJST/TS23	21	900	60,000	280[†]	Johnson et al. (2015)
28 Sep 2016	TNG/HARPS-N	40	600	115,000	110[‡]	Borsa et al. (2021)
11 Dec 2016	HJST/TS23	21	900	60,000	250[†]	This work
12 Jan 2018	TNG/HARPS-N	23	900	115,000	170[‡]	Borsa et al. (2021)
2 Jan 2019	TNG/HARPS-N	33	600	115,000	120[‡]	Borsa et al. (2021)
27 Dec 2019	OAC/MuSCAT	12	1200	65,000	50[†]	This work

[†] SNR per pixel

[‡] SNR per extracted pixel

with 21 parameters using MCMC: the λ, b and transit mid-time T_c of each epoch, $V \sin i_s$, R_p/R_s, a/R_s, two quadratic limb darkening coefficients, and the FWHM of the Gaussian line profile. The limb darkening coefficients were derived via the triangular sampling method reported in Kipping (2013), with q_1, and q_2. We estimated that q_1 and q_2 of HDS, TS23, and HIDES were equivalent. They were calculated from the stellar parameters, i.e., the effective temperature T_{eff}, surface gravity $\log g$, and metallicity. We set the priors of λ and b for all epochs and the FWHM as uniform functions while that of the priors of the other parameters were set as Gaussian priors. For the values and widths of the Gaussian priors, we set the priors for R_p/R_s and a/R_s based on the values and uncertainties reported in Kovács et al. (2013); the priors of each T_c of each epoch from P_{orb} in von Essen et al. (2014) and T_0 in von Essen et al. (2019); those of q_1, and q_2 calculated via PyLDTk (Parviainen & Aigrain 2015; Husser et al. 2013); and those of $V \sin i_s$ from Johnson et al. (2015).

For the fitting, we maximised the logarithm of the posterior probability, $\ln L_{post}$:

$$\ln L_{post} = -\sum_i \frac{(O_i - C_i)^2}{\sigma_i^2} - \sum_j \frac{(p_j - \mu_j)^2}{s_j^2}, \qquad (1)$$

where O_i is the data, C_i is the model, σ_i is the error for the ith data point, p is the parameter value at the gained iteration of the Markov chain, μ is the value from the literature, and s is the uncertainty from the literature. Index j denotes the parameters of the Gaussian priors. We set the range of the uniform prior of each λ to $-180\deg < \lambda < -90\deg$ and that of each b as $-1 < b < 1$. To converge these parameter values, we ran 4,000 steps, cut off the first 2,000 steps as burn-in, and iterated this set 100 times. Figures A1 and A2 in Appendix A plot the posterior distributions.

3 PHOTOMETRIC MEASUREMENT

3.1 Photometric Observations of WASP-33b's Transit

We observed the transit of WASP-33b by photometry using two instruments with multicolour simultaneous cameras: Multicolor Simultaneous Camera for studying Atmospheres of Transiting exoplanets (MuSCAT; Narita et al. 2015) on the 188 cm telescope at OAC and MuSCAT2 (Narita et al. 2019) on the Telescopio Carlos Sánchez (TCS) 1.52 m telescope at the Teide Observatory (OT). MuSCAT has three channels for the g'_2 (400-550 nm), r'_2 (550-700 nm), and $z_{s,2}$ (820-920 nm) bands. In contract, MuSCAT2 contains four channels for the g'_2, r'_2, $z_{s,2}$, and i'_2 (700-820 nm) bands. These bands are the Astrodon Photometrics Generation 2 -type Sloan filters. We obtained the dataset from MuSCAT on 5 November 2017 UT. We

set the exposure times of the g'_2, r'_2 and $z_{s,2}$ bands for 4, 4, and 10 s, respectively. We also obtained the dataset from MuSCAT2 on 11 October 2018 UT. The exposure time of the g'_2, r'_2, i'_2, and $z_{s,2}$ was 3, 2, 5, and 12 s, respectively.

To produce the light curves of WASP-33b, aperture photometry was performed using the pipeline proposed by Fukui et al. (2011). This process determines the stellar barycentre in every frame. We used BD+36 488, the second brightest star image in the frame, as a companion star to correct the atmospheric extinction. Next, the pipeline calculated the shift in the stellar position relative to the reference frame. This approach photometers the target star and a comparison star with a fixed aperture radius. Here, we set the aperture radii to 36 and 40 pixels for MuSCAT and MuSCAT2, respectively. After the sky background in the torus area centred on the stellar barycentr, the pipeline subtracted the sky background from WASP-33b's flux and that of the comparison. Finally, the WASP-33b light curve was obtained by dividing its flux by the comparison star flux.

3.2 Light Curve Fitting

To measure WASP-33b's impact parameter b in 2017 and 2018, we constructed light curve models with a Gaussian process using the Python code `exoplanet` (Foreman-Mackey et al. 2020). WASP-33b's light curve not only showed dimming by the transit, but also a short sinusoidal-wave-like feature due to the stellar pulsations. Thus, following a previous study by Johnson et al. (2015), we applied a Matern 3/2 kernel $\mathbf{K_{ker}}$, whose element is expressed as follows:

$$k_{i,j} = \alpha^2 \left(1 + \frac{\sqrt{3}|t_i - t_j|}{l}\right) \exp\left(-\frac{\sqrt{3}|t_i - t_j|}{l}\right) + \sigma_i^2 \delta_{i,j} \qquad (2)$$

for the Gaussian process. i and j denote the orders of the photometric observation's data, t_i and t_j are the observation times, α and l are the hyper parameters indicating the amplitude and timescale of the stellar variations, respectively, and σ is the error of data point i.

We then fitted the light curves on two epochs to the models with the following 30 parameters using MCMC: baseline B for each light curve, b and T_c of each epoch, two quadratic limb darkening coefficients u_1, u_2, and α of each band, R_p/R_s, P_{orb}, a/R_s, and l. We set the priors of B and b for both epochs, and R_p/R_s as uniform functions. We then set the priors of T_c for each epoch, u_1, u_2, and α for each band, P_{orb}, a/R_s, and l as Gaussian priors. For the values and widths of the Gaussian priors, we referred to the values and widths of Gaussian priors from Johnson et al. (2015) for α and l and von Essen et al. (2014) for P_{orb}; the others were obtained in the same manner as the spectral analysis. We set the logarithm of the likelihood $\ln P_{like}$

as

$$\ln P_{\text{like}} = -\frac{1}{2}(\ln |\mathbf{K_{ker}}| + \mathbf{r^T K_{ker}^{-1} r}) \tag{3}$$

because we adopted Gaussian process for this fitting (Rasmussen & Williams 2005). Here, $\mathbf{r}$ is a series of residuals obtained by subtracting the model data from the observation data. In the MCMC process in PyMC (Salvatier et al. 2016), we ran 1,000 steps, cut off the first 500 steps as burn-in, and iterated this set 20 times. Figures A3 and A4 in Appendix A plot the posterior distributions.

4 FITTING WITH NODAL PRECESSION MODEL

The angular momentum of WASP-33b's planetary orbit $|\overrightarrow{L_P}|$ (= $2\pi M_p a^2/P_{\text{orb}}$) is significantly smaller than the stellar rotational angular momentum of its host star $|\overrightarrow{L_s}|$; $|\overrightarrow{L_P}|/|\overrightarrow{L_s}|$ is ∼ 0.05 using the values of $|\overrightarrow{L_s}|$ from Iorio (2011), those of M_p from Lehmann et al. (2015), a, and P from Collier Cameron et al. (2010). In this case, we can regard the stellar rotational axis as a stable vector and calculate the changes in b and λ

$$b(t) = \frac{a}{R_s}(\cos\psi\cos i_s + \sin\psi\sin i_s\cos\theta(t)) \tag{4}$$

$$\tan\lambda(t) = \frac{\sin\psi\sin\theta(t)}{\sin\psi\cos i_s\cos\theta(t) - \cos\psi\sin i_s}. \tag{5}$$

Here θ, the nodal angle, can be expressed as follows:

$$\theta(t) = -\frac{3\pi J_2 R_s^2 \cos\psi}{P_{\text{orb}} a^2} t + \theta_0, \tag{6}$$

where the slope of Equation 6 is the precession speed from Barnes et al. (2013).

We then fitted the model in Equations 4 and 5 with the values measured by the MCMC using PyMC. We considered ψ, $\theta(t = 2008)$, i_s, and J_2 as free parameters and set their priors as uniform functions. Here, we set θ in 2008 as θ_0, i.e., the initial value of θ in Equation 6. For this fitting, we set the logarithm of the likelihood $\ln P_{\text{like}}$ as:

$$\ln L_{\text{like,pre}} = -\frac{1}{2}\sum_i \frac{(O_{\text{mes},i} - C_{\text{mod},i})^2}{\sigma_{\text{mes},i}^2} \tag{7}$$

where $O_{\text{mes},i}$ is the measured value of λ and b of each epoch, $C_{\text{mod},i}$ is the model value of λ and b, and $\sigma_{\text{mes},i}$ is the uncertainty of the measured λ and b, respectively. We consider that the values b in 2017 and 2018 were zero, as shown in Figure A3. We ran 20,000 steps, cut off the first 10,000 steps as burn-in, and iterated this set 20 times. The posteriors from the MCMC are shown in Figure 5, and the values are listed in Table 3. Figure 6 exhibits the changes in λ and b for WASP-33b.

5 RESULTS

Figure 2 shows the line profile residuals and the best-fitted filtered models. Table 2 lists the best values of λ and b. Our results for λ and b in 2014 were in excellent agreement with the values of Johnson et al. (2015) within 1σ, whereas those in 2008 were marginally consistent with Johnson et al. (2015) within 2σ. Moreover, our results for λ in 2016 and 2018 from HARPS-N were consistent with those of Borsa et al. (2021), whereas our λ in 2019 from HARPS-N differs from that in Borsa et al. (2021) by ∼ 2σ.

Figures 3 and 4 show the best-fit light curve models. Table 2 lists the ranges of b from MuSCAT and MuSCAT2. The posteriors of

both b in Figure A3 exhibit a truncated normal distribution with a minimum value of ∼ 0. Hence, we set 1σ as a 68% confidence interval based on the minimum value of 0 because they were identical, but with opposite signs of impact parameters, which yielded the same transit light curves.

Moreover, Figure 5 presents posteriors from MCMC with the nodal precession model. Table 3 lists the values of ψ, $\theta(t = 2008)$, i_s, and J_2. Here, we note that Iorio (2016) may have considered ψ as a variable value. Figure 6 shows the change in λ and b for WASP-33b.

6 DISCUSSION

We have inspected the nodal precession of WASP-33b with more observations than that used in previous studies (Johnson et al. 2015; Watanabe et al. 2020; Borsa et al. 2021). This is the first study to verify the nodal precession based on both Doppler tomographic observatioadds and transit photometry. The errors from the transit photometric observations were large. However, with the change in the impact parameter (see the left bottom part in Figure 6), the results from the transit photometry were consistent with the predicted values from the decreasing trend for the Doppler tomographic observations. This indicates that transit photometry can simultaneously contribute to the measurements of the nodal precession using Doppler tomographic data. In Figure 6, although the impact parameter of WASP-33b appeared to change linearly, the change in λ may not be along the model of the nodal precession. Thus, we should observe WASP-33b via Doppler tomography to clarify whether its λ increases based on the model or decreases from 2021.

6.1 Comparison of Stellar Spin Inclination and Quadrupole Moment with Previous Studies

Our i_s value disagrees with those in previous studies (Johnson et al. 2015; Iorio 2016; Watanabe et al. 2020; Borsa et al. 2021), as derived from the nodal precession by ∼3 σ or more. However, our value is similar to that of Dholakia et al. (2021), despite values that are ∼2 σ different. Notably, Dholakia et al. (2021) derived WASP-33b's i_s from light curve TESS photometric data considering its oblateness and gravity darkening.

The derived stellar quadrupole moment of WASP-33b was $J_2 = (1.36^{+0.15}_{-0.12}) \times 10^{-4}$. This value agrees with that of Iorio (2016) within 1.5 σ, which is larger than those of the other previous studies (add> 3 σ) and smaller than the theoretical value ($J_2 = 3.8 \times 10^{-4}$) calculated by Iorio (2011).

One of the possible reasons for disagreements with the values of i_s and J_2 could be the difference in the nodal precession model. Iorio (2016) and Watanabe et al. (2020) used time variation models for other orbital parameters: the ascending node Ω and the orbital inclination to the apparent equatorial plane I, illustrated in Figure 4 of Watanabe et al. (2020), and calculated from λ and b. Then, Borsa et al. (2021) estimated the change in the inclination angle $i_P (= \arccos(bR_s/a))$ as a linear function. In this study, we directly used the accurate time variation models of λ and b, such that our derived values for i_s and J_2 would be more accurate than those in previous studies. However, we should clarify the cause of the short-term variation of λ to create more detailed nodal precession model.

In contrast, there is a probability that adding datasets also causes the disagreements. In this study, we found a short-term variation in λ, which may have been decreasing since 2016, although the reason remains unclear. Therefore, we have to obtain more datasets of WASP-33b's transits to more accurately determine their values.
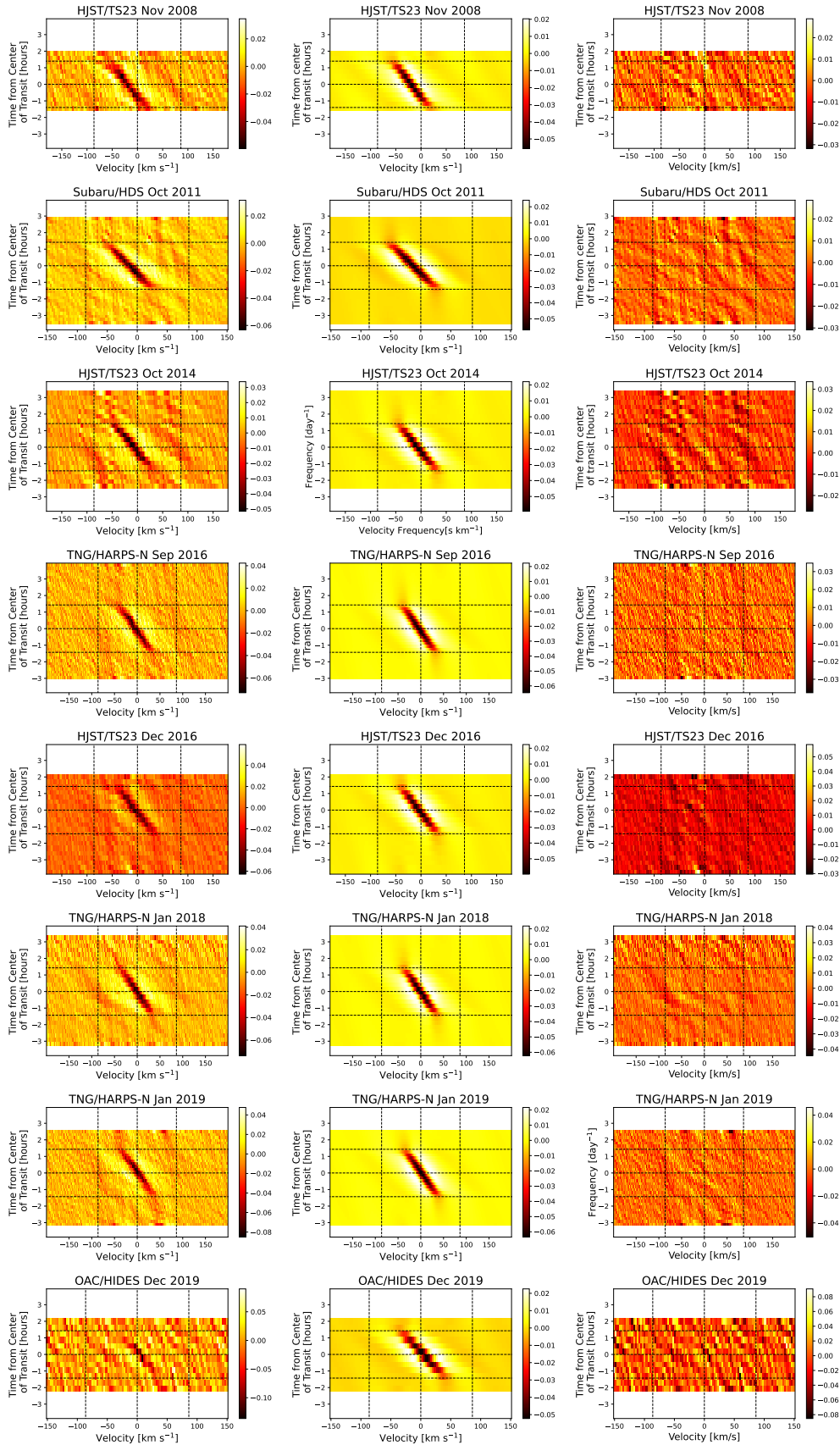
Figure 2. Fitting of the filtered residual data by MCMC. Same type of colour scale as that in the left column of Figure 1. Left column: residual data remaining as a planetary shadow. Middle column: filtered models of a planetary shadow using the best-fit values. Right column: the difference between the first row and the second rows.
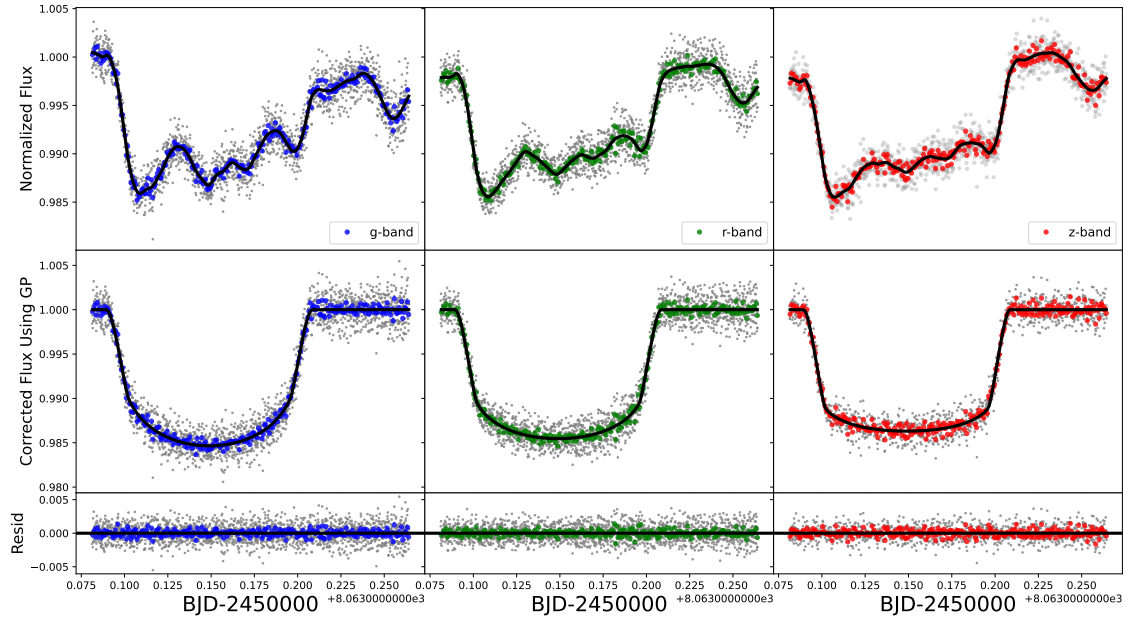
Figure 3. Light curves of MuSCAT in 2017 with the original cadences (gray points) and 1-minute bins (coloured points). Top row: light curves from the photometric observation data. The black solid lines represent the models from the MCMC fitting. Middle row: light curves subtracted using the Gaussian process. Bottom row: residuals between the observed data and model data.
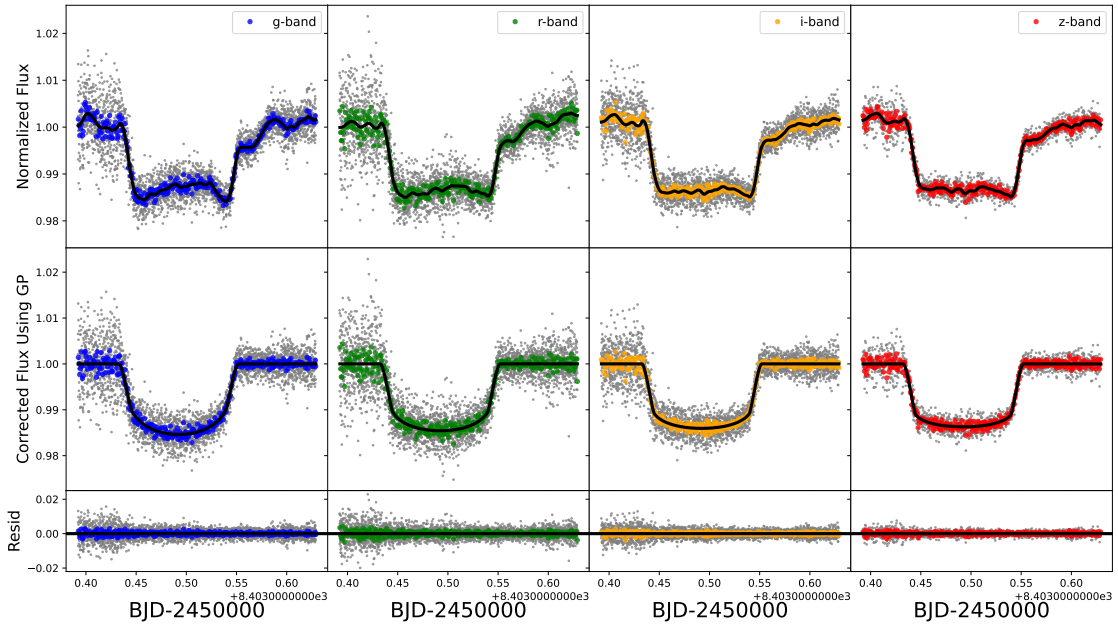

Figure 4. Similar light curves as Figure 3, but for the MuSCAT2 dataset.

Table 2. Measured parameters for WASP-33b

Date (UT)	λ (deg)	b	T_c (BJD$_{\rm TDB}$)	Method	Instrument
12 Nov 2008	$-111.30^{+0.76}_{-0.77}$	$0.2398^{+0.0062}_{-0.0058}$	$2454782.92502 \pm 0.00016$	Doppler tomography	HJST/TS23
19 Oct 2011	-113.96 ± 0.30	0.1578 ± 0.0027	$2455853.96863^{+0.00014}_{-0.00015}$	Doppler tomography	Subaru/HDS
4 Oct 2014	-113.00 ± 0.37	$0.0845 \pm +0.0031$	$2456934.77139 \pm 0.00015$	Doppler tomography	HJST/TS23
28 Sep 2016	-111.39 ± 0.23	0.0413 ± 0.0019	$2457660.59250 \pm 0.00014$	Doppler tomography	TNG/HARPS-N
11 Dec 2016	$-111.32^{+0.49}_{-0.47}$	0.0432 ± 0.0039	$2457733.78452 \pm 0.00015$	Doppler tomography	HJST/TS23
5 Nov 2017	-	$|b| < 0.132$	$2458063.14903 \pm 0.00015$	Photometry	OAC/MuSCAT
11 Oct 2018	-	$|b| < 0.067$	$2458403.49234 \pm 0.00014$	Photometry	TCS/MuSCAT2
12 Jan 2018	-111.46 ± 0.28	$0.0034^{+0.0024}_{-0.0023}$	$2458131.46135 \pm 0.00015$	Doppler tomography	TNG/HARPS-N
2 Nov 2019	-111.64 ± 0.28	$-0.0272^{+0.0020}_{-0.0021}$	$2458486.44296 \pm 0.00016$	Doppler tomography	TNG/HARPS-N
27 Dec 2019	$-112.24^{+0.97}_{-1.02}$	$-0.0592^{+0.0066}_{-0.0065}$	$2458845.08379^{+0.00015}_{-0.00016}$	Doppler tomography	OAC/HIDES

Table 3. Calculated parameters for WASP-33b

Date	ψ (deg)	J_2	i_s (deg)	θ_{2008} (deg)
Results of this study	$108.19^{+0.95}_{-0.97}$	$(1.36^{+0.15}_{-0.12}) \times 10^{-4}$	$58.3^{+4.6}_{-4.2}$	$73.6^{+1.7}_{-1.5}$
Iorio (2016)	99^{+5}_{-4} (in 2008), 103^{+5}_{-4} (in 2014)	$(2.1^{+0.8}_{-0.5}) \times 10^{-4}$	142^{+10}_{-11}	-
Watanabe et al. (2020)	-	$(9.14 \pm 0.51) \times 10^{-5}$	96^{+10}_{-14}	-
Borsa et al. (2021)	113.99 ± 0.22	$(6.73 \pm 0.22) \times 10^{-5}$	90.11 ± 0.12	-
Dholakia et al. (2021)	$108.3^{+19.0}_{-15.4}$	-	$69.8^{+4.0}_{-3.2}$	-
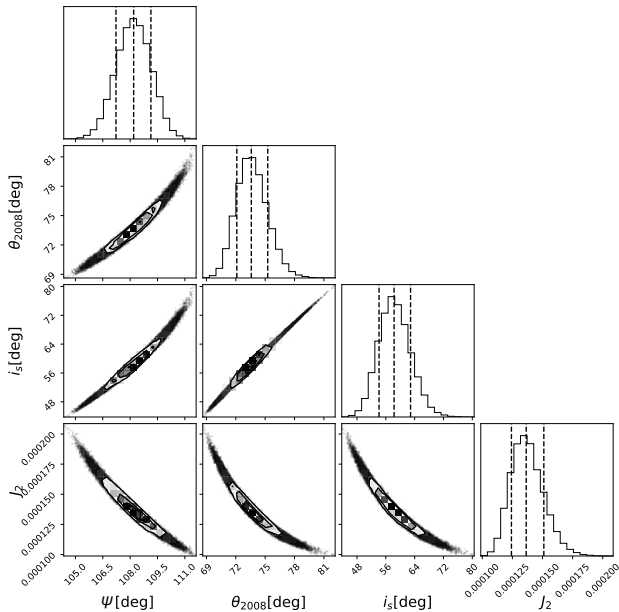
Figure 5. MCMC corner plots for the architecture angles, ψ, θ_{2008} and i_s, and stellar quadrupole moment J_2 of the WASP-33b System

6.2 Orbital Evolution of WASP-33b

We found the real spin-orbit obliquity of WASP-33b $\psi = 108.19^{+0.95}_{-0.97}$ deg. This uncertainty is larger than that reported by Borsa et al.

(2021) owing to the difference in the precession model, which shows that $d\lambda/dt$ of WASP-33b is always positive, while that of Borsa et al. (2021) allows $d\lambda/dt = 0$ at a certain time. The derived value indicates the possibility that WASP-33b has experienced the planet-planet scattering (Chatterjee et al. 2008) or Kozai migration (Fabrycky & Tremaine 2007), which are the mechanisms that cause the misaligned orbit. The existence of the WASP-33b's companion star is necessary for clarify distinguishing these two evolutionary models. Nevertheless, Doppler tomographic observations and transit photometry cannot detect the companion stars.

Ngo et al. (2016) found a companion candidate for WASP-33, estimated as a dwarf star or brown dwarf and located at 238 AU ($P_{\rm orb} \sim 3,300$ yrs) from the host star based on direct imaging. However, this candidate has not yet been confirmed owing to negligible proper motion. Thus, additional direct imaging observations are required to confirm whether the companion moves in the same proper motion as the host star or not. If the stellar companion candidate, with $0.1\,M_\star$, revolves in a circular orbit ($e = 0$) and WASP-33b was formed near the snow line, ~ 5 AU ($P_{\rm orb} \sim 12$ yrs), the planet experienced a Kozai oscillation with the Kozai cycle period, $P_{\rm Kozai}$, of 13 Myrs based on the following expression:

$$P_{\rm Kozai} = \frac{M_s P_c^2}{M_c P_b}(1 - e_c^2)^{3/2}, \tag{8}$$

where M_s, M_c, P_c, P_b, and e_c are the stellar mass, companion's mass, companion's period, planetary mass, and companion's eccentricity, respectively (Wu et al. 2007). Although we have to consider that the distance from the host star to the companion star is the sky-projected distance and the eccentricity of the companion star may exist, the Kozai cycle period could be shorter than the age of WASP-
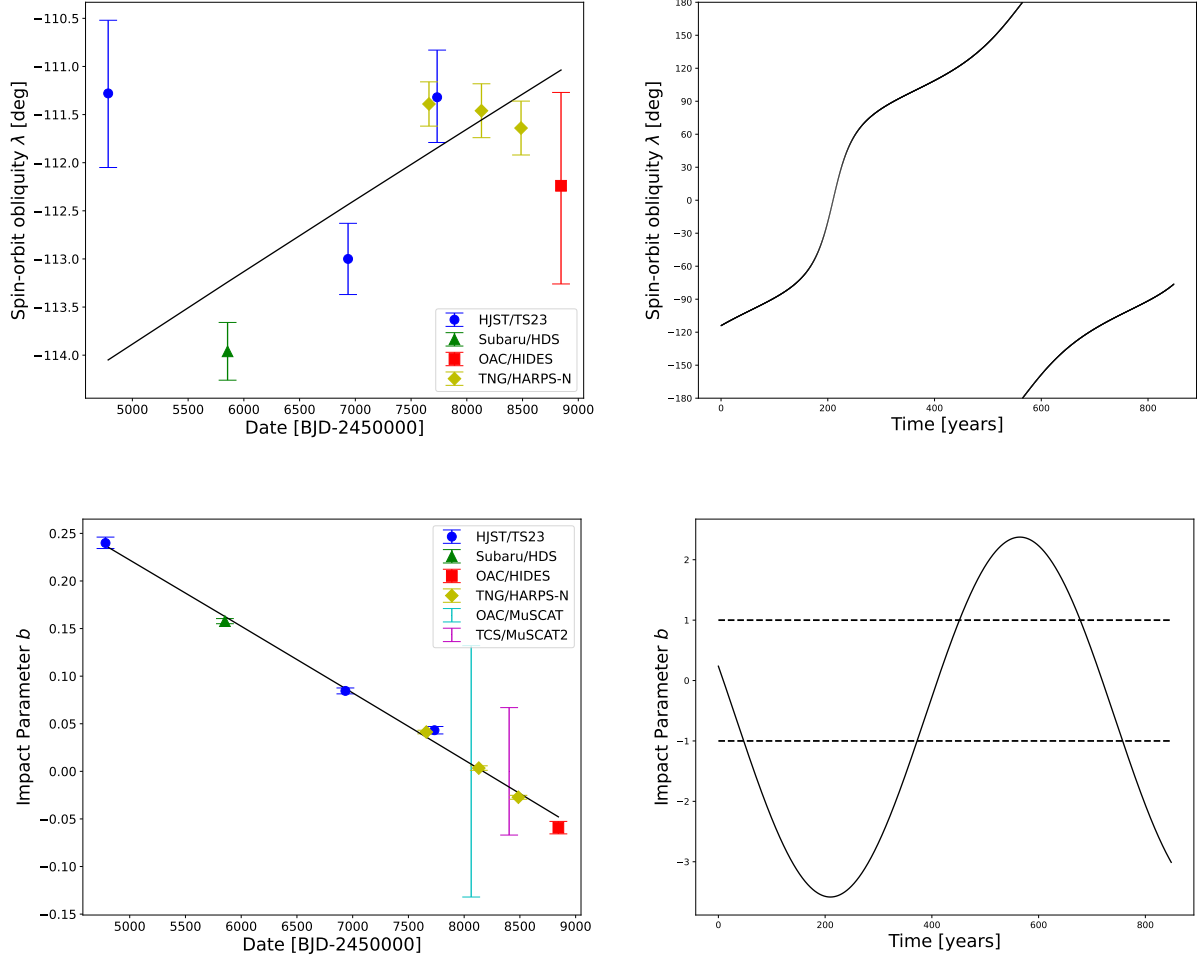
Figure 6. Changes in λ (upper row) and b (lower row). The left and right columns show the the short- and long-term changes, respectively. The x-axis of the right column is the time in years from the epoch of 2008. The blue circles show values from the HJST/TS23 datasets, the green triangles are values from Subaru/HDS, the red squares are values from OAC/HIDES, the cyan line is the value range from OAC/MuSCAT, the magenta line is the value range from TCS/MuSCAT2, and the black solid lines represent the model. In the bottom-right figure, the two black-dashed lines show the edges of the stellar disk of WASP-33b.

33 (~ 100 Myrs). Therefore, the stellar companion may have caused the Kozai mechanism for WASP-33b.

6.3 Nodal Precession Speed

We calculated the nodal precession speed $\dot{\theta} = 0.507^{+0.025}_{-0.022}$ deg year^{-1} and its period $P_{\mathrm{pre}} = 709^{+33}_{-34}$ years, where the precession was faster than that of Iorio (2016) ($\dot{\theta} = 0.37^{+0.04}_{-0.03}$). we then found that WASP-33b transits in front of the host star for only ~ 20 % of the entire nodal precession period, which indicates that it is rare to discover WASP-33b as a transiting planet. This implies that WASP-33b began transiting in 1977 $\pm$ 2 and will stop transiting in 2055 $\pm$ 2.

6.4 Nodal Precession Observations of Other Hot Jupiters around Hot Stars

Doppler tomography has confirmed 17 hot Jupiters around hot stars to date. The real spin-orbit obliquities of seven of these planets (WASP-33b, Kepler-13Ab, KELT-9b, KELT-17b, MASCARA-1b, MASCARA-4b, and WASP-189b) have been identified thus far,

which are nearly vertical (60 deg < ψ < 120 deg). The remaining hot Jupiters reveal that only their projected spin-orbit obliquities were obtained. Three hot Jupiters around hot stars with $\lambda \sim 90$ deg, i.e., KELT-26b ($\lambda = 91.3^{+6.5}_{-6.3}$ deg; Rodríguez Martínez et al. 2020), HAT-P-70b ($\lambda = 113.1^{+5.1}_{-3.4}$ deg; Zhou et al. 2019), and TOI-1518b ($\lambda = -119.66^{+0.98}_{-0.93}$ deg; Cabot et al. 2021), are valuable for detecting their observable nodal precessions to derive their ψ. Even if λ is near 0 deg or 180 deg, we can observe the change in the transit trajectory and measure ψ near 90 deg when the star rotates nearly pole-on for the line of sight. However, when λ is near 0 or 180 deg and the star rotation axis is almost perpendicular to the line of sight, the transit trajectory barely moves because ψ should also be near 0 deg or 180 deg. In this case, we can estimate ψ as λ. Therefore, we should regularly observe the nodal precessions of these planets around their hot stars to measure their ψ using Doppler tomography and transit photometry.

Kepler-13Ab, orbiting around an A-type star, is the another hot Jupiter whose nodal precession has been detected by only transit photometries (Szabó et al. 2011; Barnes et al. 2011). Previous studies have measured ψ of this hot Jupiter via gravity-darkened transit

photometry, but the values were different between these two results ($\psi = 60 \pm 2$ deg in Masuda (2015) and $\psi = 29 \pm 1$ deg in Herman et al. (2018)). Although Kepler-13Ab is likely to have evolved with Kozai migration owing to its companion star, Kepler-13B (Santerne et al. 2012), the value of its ψ should be verified by adding Doppler tomographic observations and transit photometries to obtain an accurate histogram of the derived ψ. As Johnson et al. (2014) measured the λ of Kepler-13Ab in 2014 via Doppler tomography, an additional transit spectroscopic observation enabled us to detect the change in λ and then to derive its ψ independently from the gravity-darkened transit photometry.

Ahlers et al. (2020b), Lendl et al. (2020), Ahlers et al. (2020a), and Hooton et al. (2021) measured the ψ of MASCARA-4b ($\psi = 104^{+7}_{-13}$ deg), WASP-189b ($\psi = 85.4 \pm 4.3$ deg), KELT-9b ($\psi = 87^{+10}_{-11}$ deg), and MASCARA-1b ($\psi = 72.1^{+2.5}_{-2.4}$ deg), respectively, using gravity-darkened transit photometry. Zhou et al. (2016) derived the ψ of KLET-17b ($\psi = 116 \pm 4$ deg) by the technique using the differential rotation of a host star.

These planets are hot Jupiters around A-type stars: their nodal precessions are yet to be detected. Observing the nodal precessions of these hot Jupiters is important for verifying the values of their ψ. This observation can also contribute to the investigations on the internal structure of hot stars by deriving the values of their J_2.

Although there are 17 hot Jupiters around hot stars whose projected spin-orbit obliquities have been measured, this number remains too small to statistically determine the orbital evolution tendency. Albrecht et al. (2021) found that planets around solar-like stars with large projected spin-orbit obliquities are likely to revolve on polar orbits ($\psi \sim 90$ deg); however, the tendency remains unclear for hot Jupiters around hot stars because the real spin-orbit obliquities of only six of them have been revealed. If normal planet-disk interaction is the main migration, the distribution should gather at $\psi = 0$ deg (Lai et al. 2011). If the orbital evolution by planet-planet scattering is the majority, the orbits are likely to incline at approximately $\psi = 60$ deg (Nagasawa & Ida 2011). When Kozai migration is the primary evolution, ψ has a wide range from 10 deg to 140 deg (Petrovich 2015). As Barclay et al. (2018) predicted that the TESS mission could find 500 hot Jupiters around A-type stars from the 2-year observation, increasing the number of hot Jupiters around hot stars will become possible by validating TESS planet candidates. Further observations could lead to uncovering the detailed ψ distribution around hot stars.

7 CONCLUSION

We analysed the nodal precession of WASP-33b via Doppler tomography and transit photometry using various high-dispersion spectrographs including Subaru/HDS, HJST/TS23, OAC/HIDES, and TNG/HARPS-N, and two multicolour simultaneous cameras, OAC/MuSCAT and TCS/MuSCAT2. Based on the observed change in the projected spin-orbit obliquity λ and the impact parameter b, we modelled the nodal precession of WASP-33b and derived the real spin-orbit obliquity of WASP-33b as $\psi = 108.19^{+0.95}_{-0.97}$ deg. Compared with the results of previous studies, the results of the near-polar orbit did not change. However, our value for ψ differed from that of Borsa et al. (2021) by $> 3\sigma$. This discrepancy may be caused by whether or not psi is a constant value. We assumed psi as a constant while Borsa et al. (2021) did not; Borsa et al. (2021) adopted psi from its value at the 2011 epoch. We also simultaneously derived the stellar spin inclination and the stellar gravitational quadrupole moment of WASP-33 as $i_s = 58.3^{+4.6}_{-4.2}$ deg, and $J_2 = (1.36^{+0.15}_{-0.12}) \times 10^{-4}$, respectively. These results differed by $> 3\sigma$ from those of previous

studies on nodal precession, except for the J_2 value reported in Iorio (2016) ($\sim 2.1\sigma$).

A likely reason for these discrepancies is the different nodal precession models. For the first time, we applied the accurate time variation models for λ and b to fit the nodal precession. Therefore, our derived values of ψ, i_s, and J_2 are the most accurate to date. Moreover, additional datasets may have updated these parameter values, thus causing these differences. Thus, acquiring more datasets will allow for the derivation of more accurate values of ψ, i_s, and J_2.

We calculated the nodal precession speed $\dot\theta = 0.507^{+0.025}_{-0.022}$ deg year^{-1} and its period $P_{\mathrm{pre}} = 709^{+33}_{-34}$ years, which revealed that WASP-33b transits in front of the host star for only ~ 20 % of the entire nodal precession period. Based on this result, we speculate that WASP-33b began transiting in 1977$\pm$2; we forecast that it will finish transiting in 2055$\pm$2.

The TESS survey should help us increase our ability to count number of hot Jupiters around hot stars in the future. Applying the proposed methodology to newly discovered hot Jupiters around hot stars is important not only for characterising each planetary system, but also for discriminating the migration mechanisms of such planets and investgating the internal structure of hot stars.

DATA AVAILABILITY

The raw data from OAC/HIDES, OAC/MuSCAT and TCS/MuSCAT2 will be shared on reasonable request to the

corresponding author. The reduced data of Subaru/HDS were provided by N. Narita by permission, and will be shared on request to the corresponding author with permission of N. Narita. The line profile data from HJST/TS23 were provided by M. C. Johnson by permission, and will be shared on request to the corresponding author with permission of M. C. Johnson. The line profile data of TNG/HARPS-N were provided by F. Borsa by permission, and will be shared on request to the corresponding author with permission of F. Borsa.

REFERENCES

Abt H. A., Levato H., Grosso M., 2002, ApJ, 573, 359
Ahlers J. P., et al., 2020a, AJ, 160, 4
Ahlers J. P., et al., 2020b, ApJ, 888, 63
Albrecht S., et al., 2012, ApJ, 757, 18
Albrecht S. H., Marcussen M. L., Winn J. N., Dawson R. I., Knudstrup E., 2021, ApJ, 916, L1
Barclay T., Pepper J., Quintana E. V., 2018, ApJS, 239, 2
Barnes J. W., Linscott E., Shporer A., 2011, ApJS, 197, 10
Barnes J. W., van Eyken J. C., Jackson B. K., Ciardi D. R., Fortney J. J., 2013, ApJ, 774, 53
Borsa F., et al., 2021, A&A, 653, A104
Cabot S. H. C., et al., 2021, AJ, 162, 218
Chatterjee S., Ford E. B., Matsumura S., Rasio F. A., 2008, ApJ, 686, 580
Collier Cameron A., et al., 2007, MNRAS, 375, 951
Collier Cameron A., et al., 2010, MNRAS, 407, 507
Cosentino R., et al., 2012, in McLean I. S., Ramsay S. K., Takami H., eds, Society of Photo-Optical Instrumentation Engineers (SPIE) Conference Series Vol. 8446, Ground-based and Airborne Instrumentation for Astronomy IV. p. 84461V, doi:10.1117/12.925738
Dholakia S., Luger R., Dholakia S., 2021, arXiv e-prints, p. arXiv:2109.03250
Donati J.-F., Semel M., Carter B. D., Rees D. E., Collier Cameron A., 1997, MNRAS, 291, 658
Fabrycky D., Tremaine S., 2007, ApJ, 669, 1298
Foreman-Mackey D., 2016, The Journal of Open Source Software, 24
Foreman-Mackey D., Hogg D. W., Lang D., Goodman J., 2013, PASP, 125, 306
Foreman-Mackey D., Luger R., Czekala I., Agol E., Price-Whelan A., Brandt T. D., Barclay T., Bouma L., 2020, exoplanet-dev/exoplanet v0.4.0, doi:10.5281/zenodo.1998447, https://doi.org/10.5281/zenodo.1998447
Fukui A., et al., 2011, PASJ, 63, 287
Herman M. K., de Mooij E. J. W., Huang C. X., Jayawardhana R., 2018, AJ, 155, 13
Herrero E., Morales J. C., Ribas I., Naves R., 2011, A&A, 526, L10
Hooton M. J., et al., 2021, arXiv e-prints, p. arXiv:2109.05031
Husser T.-O., Wende-von Berg S., Dreizler S., Homeier D., Reiners A., Barman T., Hauschildt P. H., 2013, A&A, 553, A6
Iorio L., 2011, Ap&SS, 331, 485
Iorio L., 2016, MNRAS, 455, 207
Izumiura H., 1999, Publications of the Yunnan Observatory, pp 77–81
Johnson M. C., Cochran W. D., Albrecht S., Dodson-Robinson S. E., Winn J. N., Gullikson K., 2014, ApJ, 790, 30
Johnson M. C., Cochran W. D., Collier Cameron A., Bayliss D., 2015, ApJ, 810, L23
Kipping D. M., 2013, MNRAS, 435, 2152
Kochukhov O., Makaganiuk V., Piskunov N., 2010, A&A, 524, A5
Kovács G., et al., 2013, A&A, 553, A44
Kupka F. G., Ryabchikova T. A., Piskunov N. E., Stempels H. C., Weiss W. W., 2000, Baltic Astronomy, 9, 590
Lai D., Foucart F., Lin D. N. C., 2011, MNRAS, 412, 2790
Lehmann H., Guenther E., Sebastian D., Döllinger M., Hartmann M., Mkrtichian D. E., 2015, A&A, 578, L4
Lendl M., et al., 2020, A&A, 643, A94
Masuda K., 2015, ApJ, 805, 28

Nagasawa M., Ida S., 2011, ApJ, 742, 72
Narita N., et al., 2015, Journal of Astronomical Telescopes, Instruments, and Systems, 1, 045001
Narita N., et al., 2019, Journal of Astronomical Telescopes, Instruments, and Systems, 5, 015001
Ngo H., et al., 2016, ApJ, 827, 8
Noguchi K., et al., 2002, Publications of the Astronomical Society of Japan, 54, 855
Parviainen H., Aigrain S., 2015, MNRAS, 453, 3821
Pepper J., et al., 2007, PASP, 119, 923
Petrovich C., 2015, ApJ, 799, 27
Rasmussen C. E., Williams C. K. I., 2005, Gaussian Processes for Machine Learning (Adaptive Computation and Machine Learning). The MIT Press
Ricker G. R., et al., 2015, Journal of Astronomical Telescopes, Instruments, and Systems, 1, 014003
Rodríguez Martínez R., et al., 2020, AJ, 160, 111
Salvatier J., Wiecki T. V., Fonnesbeck C., 2016, PeerJ Computer Science, 2, e55
Santerne A., et al., 2012, A&A, 544, L12
Science Software Branch at STScI 2012, PyRAF: Python alternative for IRAF (ascl:1207.011)
Szabó G. M., et al., 2011, ApJ, 736, L4
Szabó G. M., Pál A., Derekas A., Simon A. E., Szalai T., Kiss L. L., 2012, MNRAS, 421, L122
Tull R. G., MacQueen P. J., Sneden C., Lambert D. L., 1995, PASP, 107, 251
Watanabe N., Narita N., Johnson M. C., 2020, PASJ, 72, 19
Wu Y., Murray N. W., Ramsahai J. M., 2007, ApJ, 670, 820
Zhou G., et al., 2016, AJ, 152, 136
Zhou G., et al., 2019, AJ, 158, 141
von Essen C., et al., 2014, A&A, 561, A48
von Essen C., Mallonn M., Welbanks L., Madhusudhan N., Pinhas A., Bouy H., Weis Hansen P., 2019, A&A, 622, A71

APPENDIX A: MCMC RESULTS OF DOPPLER TOMOGRAPHIC AND PHOTOMETRIC MEASUREMENTS

Here, we display the corner plots after using MCMC in Section 2.3 (Figure A1 and Figure A2) and in Section 3.2 (Figure A3 and Figure A4).

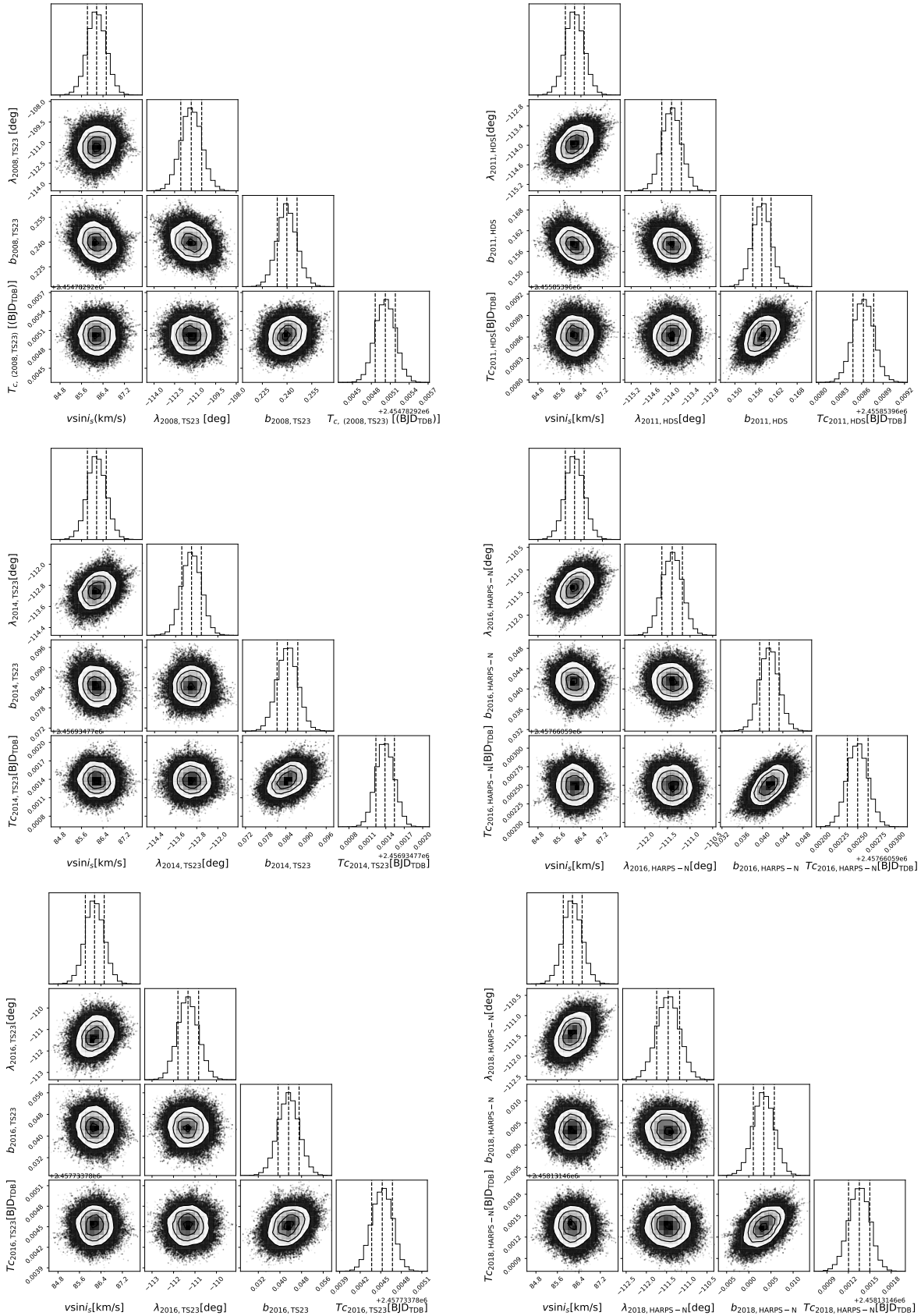This paper has been typeset from a TEX/LATEX file prepared by the author.

Figure A1. Corner plots for the free parameters after using MCMC in section 2.3. Black circles indicate 68%, 95%, and 99.7% confidence from the inside. In each posterior distribution of each parameter, the vertical dotted lines show the best-fit value (middle) and 1σ confidence (both ends). We created these plots using corner.py (Foreman-Mackey 2016).
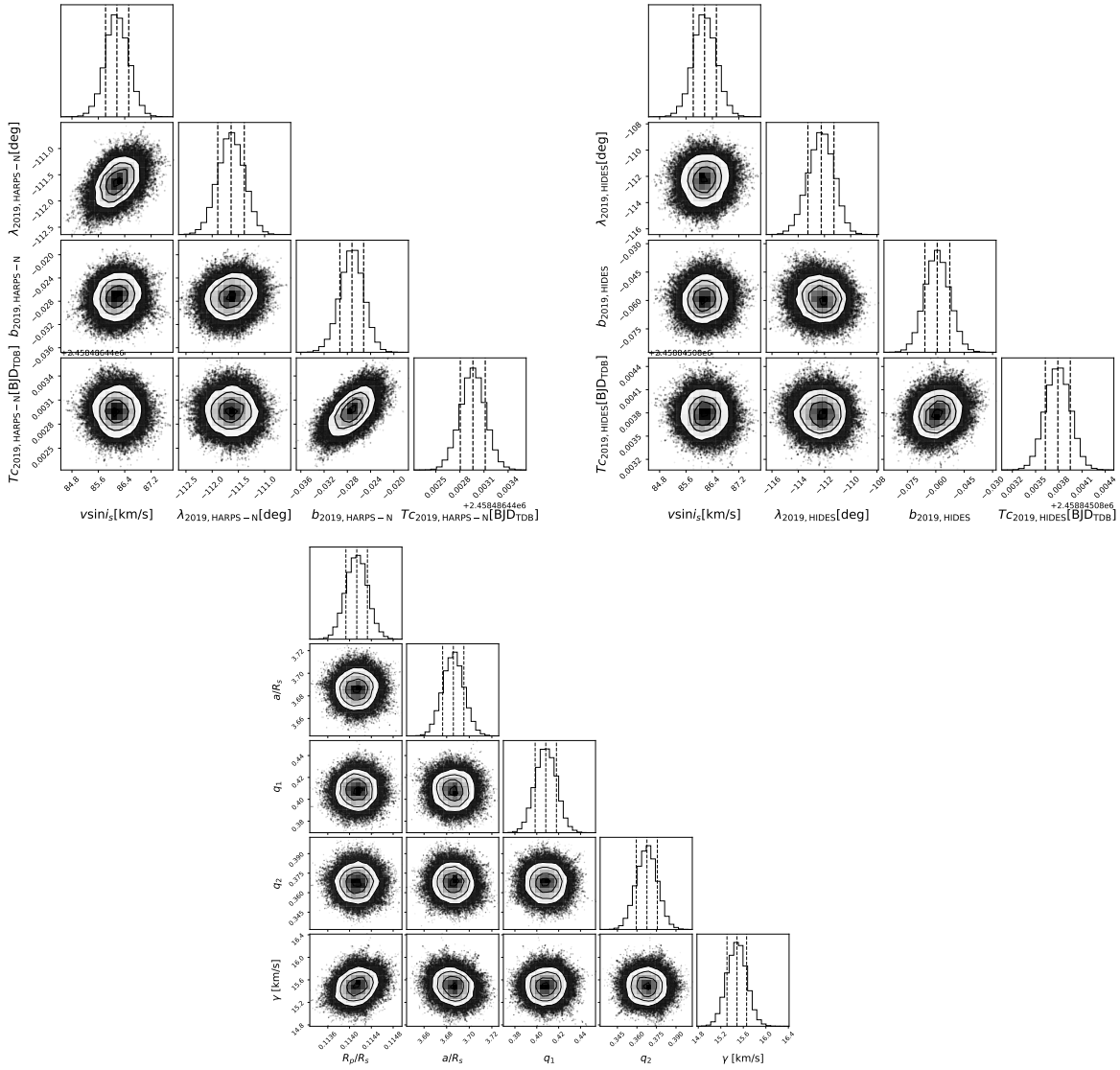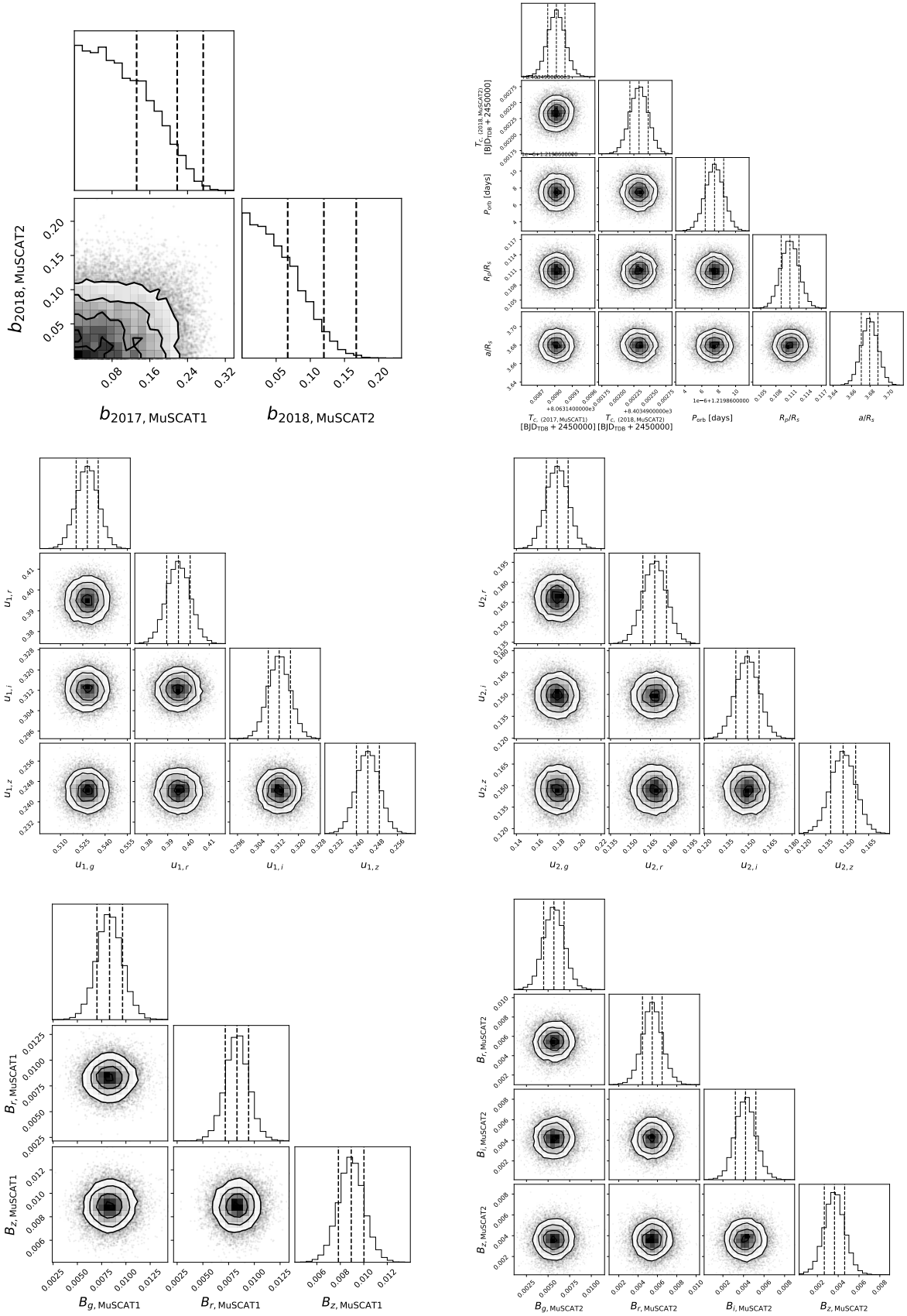
Figure A2. Continuance of Figure A1.

Figure A3. Plot distributions for impact parameter of each epoch, radial-ratio, period and transit mid-time of each epoch, limb darkening coefficients of each band, and base line of each light curve. These are the same corner plots as in Figure A1, but for the transit photometry by MuSCAT1 and MuSCAT2.
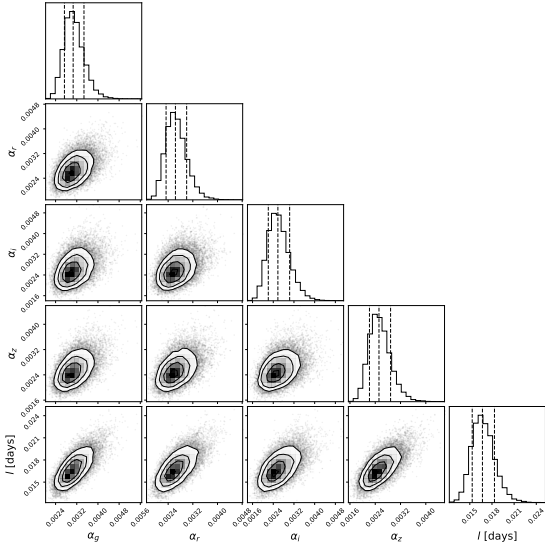
Figure A4. Continuance of Figure A3. Plot distributions for the impact parameter of each epoch, σ of each band, l, period, and transit mid-time of each epoch.